ISSN 1674-1056
http://cpb.iphy.ac.cn
http://iopscience.iop.org/cpb
中国物理 B
Chinese Physics
中国物理 Chinese Physics B

Influence exerted by bone-containing target body on thermoacoustic imaging with current injection

Yan-Hong Li(李艳红), Guo-Qiang Liu(刘国强), Jia-Xiang Song(宋佳祥), Hui Xia(夏慧)

Citation: Chin. Phys. B . 2019, 28(4): 044302. **doi:** 10.1088/1674-1056/28/4/044302
Journal homepage: http://cpb.iphy.ac.cn; http://iopscience.iop.org/cpb

What follows is a list of articles you may be interested in

Enhancement of photoacoustic tomography in the tissue with speed-of-sound variance using ultrasound computed tomography

Cheng Ren-Xiang, Tao Chao, Liu Xiao-Jun
Chin. Phys. B . 2015, 24(11): 114301. **doi:** 10.1088/1674-1056/24/11/114301

Nonlinear impedances of thermoacoustic stacks with ordered and disordered structures

Ge Huan, Fan Li, Xia Jie, Zhang Shu-Yi, Tao Sha, Yang Yue-Tao, Zhang Hui
Chin. Phys. B . 2014, 23(7): 074301. **doi:** 10.1088/1674-1056/23/7/074301

Effects of size and arrangement of virtual transducer on photoacoustic tomography

Wang Shao-Hua, Tao Chao, Liu Xiao-Jun
Chin. Phys. B . 2013, 22(7): 074303. **doi:** 10.1088/1674-1056/22/7/074303

Influence of limited-view scanning on depth imaging of photoacoustic tomography

Wu Dan, Tao Chao, Liu Xiao-Jun, Wang Xue-Ding
Chin. Phys. B . 2012, 21(1): 014301. **doi:** 10.1088/1674-1056/21/1/014301

Influence exerted by bone-containing target body on thermoacoustic imaging with current injection*

Yan-Hong Li(李艳红)[1,2], Guo-Qiang Liu(刘国强)[1,2,†], Jia-Xiang Song(宋佳祥)[1,2], and Hui Xia(夏慧)[1]

[1] *Institute of Electrical Engineering, Chinese Academy of Sciences, Beijing* 100190, *China*
[2] *University of Chinese Academy of Sciences, Beijing* 100049, *China*

(Received 30 November 2018; revised manuscript received 1 February 2019; published online 5 March 2019)

Thermoacoustic imaging with current injection (TAI-CI) is a novel imaging technology that couples with electromagnetic and acoustic research, which combines the advantages of high contrast of the electrical impedance tomography and the high spatial resolution of sonography, and therefore has the potential for early diagnosis. To verify the feasibility of TAI-CI for complex bone-containing biological tissues, the principle of TAI-CI and the coupling characteristics of fluid and solid were analyzed. Meanwhile, thermoacoustic (TA) effects for fluid model and fluid–solid coupling model were analyzed by numerical simulations. Moreover, we conducted experiments on animal cartilage, hard bone and biological soft tissue phantom with low conductivity (0.5 S/m). By injecting a current into the phantom, the thermoacoustic signal was detected by the ultrasonic transducer with a center frequency of 1 MHz, thereby the B-scan image of the objects was obtained. The B-scan image of the cartilage experiment accurately reflects the distribution of cartilage and gel, and the hard bone has a certain attenuation effect on the acoustic signal. However, compared with the ultrasonic imaging, the thermoacoustic signal is only attenuated during the outward propagation. Even in this case, a clear image can still be obtained and the images can reflect the change of the conductivity of the gel. This study confirmed the feasibility of TAI-CI for the imaging of biological tissue under the presence of cartilage and the bone. The novel TAI-CI method provides further evidence that it can be used in the diagnosis of human diseases.

Keywords: biomedical imaging, thermo-acoustic imaging, fluid–solid coupling, low conductivity

PACS: 43.35.Ud, 87.85.Pq, 43.35.Wa, 44.05.+e **DOI:** 10.1088/1674-1056/28/4/044302

1. Introduction

Cancer is the most commonly diagnosed type of serious human disease and it has the highest mortality rate.[1,2] However, current routine clinical structure imaging techniques cannot provide an early diagnosis of tumours very well, although it has been demonstrated that early detection can greatly increase the cure rate of breast cancer. Therefore, there is an urgent need to develop functional imaging techniques that enable early diagnosis. Compared with the normal tissue, the electrical characteristics of tumors are quite different in the process of occurrence and development,[3–6] while the change of electrical parameter of biological tissue often appears prior to the change of the structure.[7] Therefore, under the guidance of electrical impedance tomography (EIT), a functional imaging method based on the electrical parameter spectrum of biological tissue appears over time.[8–13]

For any imaging method, high contrast, high resolution, and enough penetration depths are important performance indexes. At present, EIT has lower sensitivity and spatial resolution, and conventional ultrasound is poor in soft tissues, which makes it difficult to reliably separate normal and malignant breast tissues.[14] A technique to obtain the electrical parameter spectrum using a single physics field will find it difficult to meet the performance requirements that encompass the entire above-mentioned indexes. Accordingly, it is desirable to meet all of the performance requirements with the help of multi-physical fields coupling methods.[15] So far, a variety of functional imaging techniques have been developed, which can be divided into two categories: the first based on magneto–acoustic effects[16–19] and the second using thermo–acoustic effects.[20–25] The latter contains photoacoustic,[26–28] microwave-induced thermo–acoustic imaging (MI-TAI),[20,23] magnetically mediated thermo–acoustic imaging (MM-TAI),[22,24] and thermo–acoustic imaging with current injection (TAI-CI), which is proposed in this paper.[25]

Compared with EIT, TAI-CI is a new multi-physical field imaging method that uses pulse current as an excitation source and can detect ultrasonic signals, which can improve the resolution and avoid the interference from contact impedance of detection electrode. A comparative study on MM-TAI and TAI-CI indicated that the magnetic acoustic effect exists in the thermo–acoustic effects.[29] The magnetic acoustic effect of TAI-CI is smaller for biological tissues than that of MM-

*Project supported by the National Natural Science Foundation of China (Grant No. 51477161), the National Key Research and Development Program of China (Grant No. 2018YFC0115200), and the Fund from the Chinese Academy of Sciences (Grant No. YZ201507).

†Corresponding author. E-mail: gqliu@mail.iee.ac.cn

© 2019 Chinese Physical Society and IOP Publishing Ltd

TAI, so TAI-CI can avoid the issue of the mixing of magneto–acoustic and thermo–acoustic effects in MM-TAI. Meanwhile, TAI-CI can also reduce the excitation source power and increase the detected signal strength.

In comparison with microwave-induced thermo–acoustic imaging, MM-TAI has the potential of deeper penetration depth. For commonly used frequencies, such as 3 GHz, the penetration depths for fat and muscle are estimated to be 9 cm and 1.2 cm, respectively, while at 500 MHz, the penetration depths are estimated to be 23.5 cm and 3.4 cm, respectively.[30,31] The excitation source of MM-TAI has a width of 1 μs and a carrier frequency at 12.4 MHz which offers at least 15-cm penetration.[22] The width of pulsed current for TAI-CI is less than 1 μs, which can further increase the penetration depth of biological tissue. Furthermore, TAI-CI can reduce the excitation source power and increase the detected signal strength on the basis of consistent security. In comparison with the magneto–acoustic tomography, TAI-CI can simplify the imaging system and reduce costs.

Up to now, the preliminary theoretical basis of TAI-CI has been formed and the experimental results of gel with low conductivity have been reported. The resolution of the imaging system can reach 2 mm when using an ultrasonic transducer with a center frequency of 1 MHz,[32] the resolution of image is higher in the recent study. In the current research on TAI-CI, the conductivity distribution acquired by acoustic pressure inversion is based on the assumption that the target is a whole fluid. However, the pure fluid model may not be suitable for the actual organism, such as head or chest, which contains solid matter. Obviously, it is necessary to investigate the influence of a complex structure on the reconstruction of an acoustic source or conductivity, starting with the acoustic field model.

The conventional ultrasonic imaging method is based on the echo principle — a beam of ultrasound is sent to the human body by the acoustic probe, and the ultrasonic reflected signal is received by the receiving probe. An image of the internal organs can then be obtained. In the process of receiving and transmitting, the ultrasonic signal is attenuated twice due to the presence of bones. The thermal expansion of the internal organs of the TAI-CI excites the thermo–acoustic signal and the ultrasonic signal is only attenuated during outward propagation. Therefore, TAI-CI is expected to optimize signal attenuation problems caused by bone decay.

In this paper, the principle of thermo–acoustic imaging with current injection and the coupling characteristics of fluid and solid are analyzed. Moreover, the thermo–acoustic effects of pure fluid model and fluid–solid coupling model are analyzed by numerical simulation. Meanwhile, the experimental system is established to test the animal cartilage, hard bone and biological soft tissue phantom with low-conductivity (0.5 S/m), and the acoustic signal is detected by an ultrasonic transducer with a center frequency of 1 MHz. The mutual verification of theory, simulation, and experiment is realized. It is further proven that this method is feasible for biological imaging. The fluid–solid coupling model developed in this research will provide an analytical means for accurate imaging in the presence of a complex biological structure.

2. Principle and method

TAI-CI is a multi-field coupling imaging method that combines electric, thermal, and acoustic techniques. A schematic diagram of TAI-CI is shown in Fig. 1. By injecting a pulse current into the object through a pair of electrodes, A and B, joule heating is produced inside the object and the acoustic signal is excited due to thermal expansion. The acoustic signal is then detected and finally the image can be reconstructed. The image can reflect the electrical parameters of the target.

Because malignant tissue can absorb more energy than normal tissue and emit stronger acoustic wave, the locations, dimensions, and morphologies of tumors can be determined from the image.

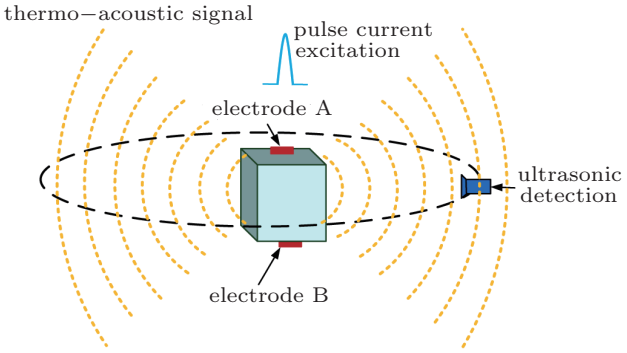


Fig. 1. Principle diagram of thermo–acoustic imaging with current injection.

2.1. Electromagnetic-field model

The electromagnetic field forward problem is as follows: the electrical conductivity of the object is a known quantity, and it is required to solve the the heat absorption distribution produced by the injection current. The acoustic field forward problem needs to solve the ultrasonic signal based on the known heat absorption distribution. The ultrasonic signal reflects the process of spreading outward of the acoustic wave.

According to the Helmholtz theorem, the electric field can be expressed as Eq. (1) under the quasi static electric approximation condition.

$$\boldsymbol{E} = -\nabla\phi, \tag{1}$$

where ϕ is an electric scalar potential.

According to the current continuity theorem, the equations of electric field and the boundary conditions of target can be described as follows:

$$\begin{cases} \nabla \cdot [\sigma(\boldsymbol{r}')\nabla\phi(\boldsymbol{r}',t)] = 0, \\ \sigma \dfrac{\partial\phi}{\partial n}\Big|_{\Gamma_{\mathrm{A,B}}} = \pm\dfrac{I(t)}{A_0}, \\ \dfrac{\partial\phi}{\partial n}\Big|_{\Gamma_{\mathrm{g}}} = 0, \\ \phi(\boldsymbol{r}',t)|_{t=0} = 0, \end{cases} \tag{2}$$

where $\Gamma_{\mathrm{A,B}}$ is the position of the electrodes, Γ_{g} is the outer boundary of the object except the electrode position, A_0 is the contact area between the electrode and object, $I(t)$ is the injection current, σ is the conductivity, and $\partial\phi/\partial n$ is the normal derivative of ϕ.

The current density distribution in an object is expressed as follows:

$$\boldsymbol{J}(\boldsymbol{r}',t) = \sigma(\boldsymbol{r}',t)\boldsymbol{E}(\boldsymbol{r}',t). \tag{3}$$

The short duration of pulse allows us to restrict the energy deposition and minimize the effect of thermal diffusion on the thermo–acoustic waves. For this thermo–acoustic imaging, the pulse duration τ_{p} is shorter than the thermal transport time of absorbed energy τ_{t}, which is referred to as thermal confinement.[33,34] The condition of thermal confinement can be expressed as $\tau_{\mathrm{p}} < \tau_{\mathrm{t}} < l^2/\alpha$, where α is the thermal diffusivity of the object and l is the penetration depth or the size of the object. Within the same amount of time, the distance of the acoustic wave propagation is longer than the length of the heat transfer, even if the pulse width is 1 μs.

The instantaneous short pulse excites the joule heat. The heating function can then be described by the power deposition in the object. The heating function can be written in the following

$$S(\boldsymbol{r}',t) = \sigma(\boldsymbol{r}')\left|\boldsymbol{E}(\boldsymbol{r}',t)\right|^2 + \omega\varepsilon_0\varepsilon_{\mathrm{r}}''\left|\boldsymbol{E}(\boldsymbol{r}',t)\right|^2 + \omega\mu_0\mu_{\mathrm{r}}''\left|\boldsymbol{H}(\boldsymbol{r}',t)\right|^2, \tag{4}$$

where ε_0 and μ_0 are the electric permittivity and magnetic permeability in free space, $\varepsilon_{\mathrm{r}}''$ is the imaginary part of the relative permittivity that describes the losses, μ_{r}'' is the imaginary part of the relative magnetic permeability that describes the magnetic losses within the medium, whereas $\boldsymbol{E}(\boldsymbol{r}',t)$ and $\boldsymbol{H}(\boldsymbol{r}',t)$ are the electric field and magnetic field in the medium. The first two terms describe the resistance loss and dielectric loss, which dominate in thermal energy generation in tissue. The last term is magnetic loss because normally $\mu_{\mathrm{r}}'' = 0$ in biological tissues, the magnetic loss can be negligible in tissue.[35] Then equation (4) can be rewritten as

$$S(\boldsymbol{r}',t) = \left(\sigma(\boldsymbol{r}') + \omega\varepsilon_0\varepsilon_{\mathrm{r}}''\right)\left|\boldsymbol{E}(\boldsymbol{r}',t)\right|^2. \tag{5}$$

For frequencies below 100 MHz, the resistance loss of biological materials dominates over the dielectric loss.[36] For 1 MHz, the dielectric loss can almost be ignored. Equation (5) can then be rewritten as Eq. (6). Tissue with high conductivity like muscle ($\sigma = 0.5 \sim 0.7$ S/m at 1 MHz) exhibits higher energy absorption than the tissue with low conductivity, such as fat ($\sigma = 0.02 \sim 0.03$ S/m at 1 MHz).[37,38] The results of thermo–acoustic image can reflect the conductivity distributions in the imaged object[39]

$$S(\boldsymbol{r}',t) = \sigma(\boldsymbol{r}')\left|\boldsymbol{E}(\boldsymbol{r}',t)\right|^2. \tag{6}$$

According to Refs. [20] and [33], the heating function $S(\boldsymbol{r}',t)$ can be separated into a spatial absorption function and a temporal function of the source

$$S(\boldsymbol{r}',t) = S(\boldsymbol{r}')\cdot I(t). \tag{7}$$

The short pulse can be regarded as a Dirac delta function

$$I(t) = \delta(t). \tag{8}$$

Heat absorption distribution $S(\boldsymbol{r}')$ is the total energy absorbed at position r during the excitation with the pulse width of τ_{p}, which is an integration of $S(\boldsymbol{r}',t)$

$$S(\boldsymbol{r}') = \int_0^{\tau_{\mathrm{p}}} S(\boldsymbol{r}',t)\,\mathrm{d}t. \tag{9}$$

To demonstrate the validity of electromagnetic field model for TAI-CI, a simulation was conducted to calculate the two-dimensional (2D) distribution of the heating absorption. The geometric model is shown in Fig. 2, which is mainly divided into three regions: Ω_1, Ω_2, and Ω_3, Ω_1 and Ω_2 represent the object area, which may be the fluid area or solid area; Ω_3 represents coupling region, which can be regarded as fluid area; and $\sigma(\boldsymbol{r}')$ can be used to represent the electrical conductivity distribution of the entire area. A and B are electrodes.

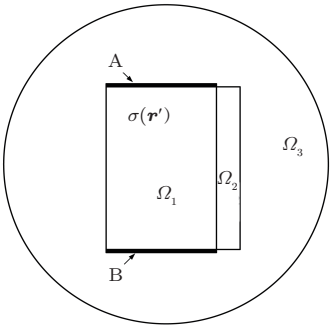


Fig. 2. The geometric model.

2.2. Acoustic-field model for a fluid

When three regions are all fluid, the fluid model can be built and solved for the acoustic problem.

Thermal diffusion in the thermo–acoustic process can be neglected because the power pulse width (0.5 μs ∼ 1 μs) is much shorter than the thermal diffusion time in water and biological tissue.

The generation and propagation of thermo–acoustic signals for TAI-CI are described by the thermo–acoustic wave equation[36]

$$\nabla^2 p(\boldsymbol{r},t) - \frac{1}{c_s^2}\frac{\partial^2 p(\boldsymbol{r},t)}{\partial t^2} = -\rho_0\beta\frac{\partial^2 T(\boldsymbol{r},t)}{\partial t^2}, \tag{10}$$

where $p(\boldsymbol{r},t)$ is acoustic pressure depending on the location of $\boldsymbol{r}$ and time of t, $T(\boldsymbol{r},t)$ is the temperature variation in space and time, c_s denotes the speed of sound, C_P and β denote the specific heat capacity at constant volume and the thermal expansion coefficient, respectively. The temperature field is governed by the heat equation

$$\rho_0 C_p\frac{\partial T(\boldsymbol{r},t)}{\partial t} - \nabla\cdot(k\nabla T) = S\left(\boldsymbol{r}',t\right), \tag{11}$$

where k is the thermal conductivity, the relationship between k and the thermal diffusivity α is

$$\alpha = \frac{k}{\rho_0 C_p}. \tag{12}$$

The ultrafast pulse excitation combined with the low values of the thermal diffusivity α in soft tissue results in faster temperature changes and negligible heat transfer

$$\nabla\cdot(k\nabla T) = 0. \tag{13}$$

Then equation (11) is reduced to

$$\rho_0 C_p\frac{\partial T(\boldsymbol{r},t)}{\partial t} = S\left(\boldsymbol{r}',t\right). \tag{14}$$

By substituting Eq. (14) to Eq. (10), one obtains

$$\nabla^2 p(\boldsymbol{r},t) - \frac{1}{c_s^2}\frac{\partial^2}{\partial t^2}p(\boldsymbol{r},t) = -\frac{\beta}{C_p}\frac{\partial S(\boldsymbol{r}',t)}{\partial t}. \tag{15}$$

The right-hand side of Eq. (15) includes the thermo–acoustic source term $\partial S(\boldsymbol{r}',t)/\partial t$. Under thermal stress confinement, using Eqs. (7) and (8), the partial derivative of heating function, which is regarded as thermo–acoustic source can be rewritten in the form

$$\frac{\partial S(\boldsymbol{r}',t)}{\partial t} \approx S\left(\boldsymbol{r}'\right)\frac{\partial\delta(t)}{\partial t}. \tag{16}$$

With product separate contribution of the spatial $S(\boldsymbol{r}')$ and temporal $\delta(t)$ parts,[39] equation (15) can be rewritten in the form

$$\nabla^2 p(\boldsymbol{r},t) - \frac{1}{c_s^2}\frac{\partial^2}{\partial t^2}p(\boldsymbol{r},t) = -\frac{\beta}{C_p}S(\boldsymbol{r}')\frac{\partial I(t)}{\partial t}. \tag{17}$$

So, for the pure fluid model the thermo–acoustic wave equation and the corresponding boundary conditions can be described as follows:

$$\begin{cases} \nabla^2 p(\boldsymbol{r},t) - \dfrac{1}{c_s^2}\dfrac{\partial^2}{\partial t^2}p(\boldsymbol{r},t) = -\dfrac{\beta}{C_p}S(\boldsymbol{r}')\dfrac{\partial I(t)}{\partial t}, \\ p(\boldsymbol{r},t)|_{t=0} = 0, \\ \left.\dfrac{\partial p(\boldsymbol{r},t)}{\partial t}\right|_{t=0} = 0, \\ p(\boldsymbol{r},t)|_{\boldsymbol{r}\to\infty} = 0. \end{cases} \tag{18}$$

The acoustic pressure $p(\boldsymbol{r},t)$ at point $\boldsymbol{r}$ can be solved according to Eq. (18)

$$p(\boldsymbol{r},t) = \frac{1}{4\pi}\int_\Omega \frac{\beta}{C_p}S(\boldsymbol{r}')\frac{\partial I(t)}{\partial t}\frac{\delta(t-R/c_s)}{R}\,\mathrm{d}\Omega', \tag{19}$$

where the expression of R is $R = |\boldsymbol{r}'-\boldsymbol{r}|$, $\boldsymbol{r}$ and $\boldsymbol{r}'$ are the position of the transducer and the sound source.

2.3. Acoustic field model for fluid–solid coupling

When the three regions include a fluid and solid, it is necessary to establish a fluid–solid coupling model and solve the coupled acoustic field problem. It is assumed that regions Ω_1 and Ω_3 are fluids and regions Ω_2 is the solid area.

In the regions Ω_1 and Ω_3, the thermo–acoustic is still governed by the thermo–acoustic wave equation [Eq. (17)]. When the vibration in the solid propagates to the interface of the fluid, the force displacement $\boldsymbol{u}$ in the solid is converted to the acoustic pressure in the fluid. Considering the solid boundary displacement effects on the fluid, the thermo–acoustic wave equation and boundary conditions in the fluid area can be described as

$$\begin{cases} \nabla^2 p(\boldsymbol{r},t) - \dfrac{1}{c_s^2}\dfrac{\partial^2}{\partial t^2}p(\boldsymbol{r},t) = -\dfrac{\beta}{C_p}S(\boldsymbol{r}')\dfrac{\partial I(t)}{\partial t}, \\ \boldsymbol{n}\cdot\nabla p(\boldsymbol{r},t)\big|_{\text{fluid–solid}} = -\rho_0\boldsymbol{n}\cdot\left.\dfrac{\partial^2\boldsymbol{u}}{\partial t^2}\right|_{\text{fluid–solid}}, \\ p(\boldsymbol{r},t)|_{t=0} = 0, \\ \left.\dfrac{\partial p(\boldsymbol{r},t)}{\partial t}\right|_{t=0} = 0, \\ p(\boldsymbol{r},t)|_{\boldsymbol{r}\to\infty} = 0. \end{cases} \tag{20}$$

When the acoustic signal encountered solid materials during the transmission process in the flow, acoustic pressure is converted to force at the interface between fluid and solid, and then the displacement produced by vibration force in a solid. When the elastic medium is in the state of stress and strain, the resultant force of physical force and surface force acting on the element should be balanced with the inertial force, the equilibrium equation, temperature field equation and the boundary

condition describing this process in the regions Ω_2 can be expressed as

$$\begin{cases} (\lambda+\mu)\nabla\nabla\cdot\boldsymbol{u}+\mu\nabla^2\boldsymbol{u}-\beta_T\nabla T=\rho_0\dfrac{\partial^2\boldsymbol{u}}{\partial t^2}, \\ f|_{\text{fluid–solid}}=-\boldsymbol{n}p|_{\text{fluid–solid}}, \\ \boldsymbol{u}(\boldsymbol{r},t)|_{t=0}=0, \\ \left.\dfrac{\partial\boldsymbol{u}(\boldsymbol{r},t)}{\partial t}\right|_{t=0}=0, \end{cases} \tag{21}$$

where $\boldsymbol{n}$ is the normal vector at the interface between fluid and solid, $\boldsymbol{u}$ is displacement produced by vibration in a solid, λ and μ are Lame coefficient, Based on Eqs. (7) and (14) the temperature can be obtained as follows:

$$T=\frac{1}{\rho_0 C_p}\int_0^{\tau_p} S\left(\boldsymbol{r}',t\right)\mathrm{d}t. \tag{22}$$

3. Numerical simulation

The geometric models for numerical simulation were established to evaluate the proposed mathematical model. The characteristics of TAI-CI were tested by simulation with different parameters of setups, fluid model and fluid–solid coupling model were both analyzed.

It is reported that the conductivity of human or animal tissues is commonly below 1.0 S/m.[40] For the same type of tissue, the differences between the electrical properties of malignant and that of normal are greatest in the mammary gland (average difference of conductivity is about 577%).[41] The conductivity of cartilage is commonly from 0.15 S/m to 0.3 S/m, and conductivity of bone is about from 0.02 S/m to 0.04 S/m in the frequency of 1 MHz.[37,38] This provides a reference for parameter selection in the simulation model.[42,43] The simulation geometric models were established to simulate normal, tumor tissue, and bone, as in Fig. 3.

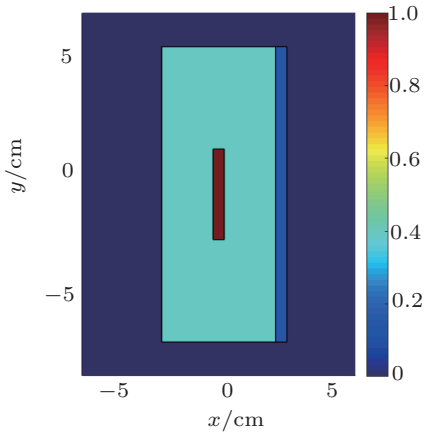


Fig. 3. Conductivity distribution.

The model was made of a rectangle measuring 50 mm × 120 mm and a concentric inner rectangle measuring 5 mm × 50 mm, the outer rectangle was used to simulate the normal tissue, and the inner rectangle was used to simulate the tumor tissue. The materials were set to muscle, and the electrical conductivity of the outer rectangle and the inner rectangle were set to 0.4 S/m and 1 S/m, respectively. There was also a rectangle measuring 5 mm × 120 mm on the right-hand side of the outer rectangle to simulate the bone — including cartilage and hard bone. To couple the acoustic field, the model should be immersed into the insulating oil — the speed of sound in the insulating oil was set to 1481 m/s. The acoustic system was set to be uniform without consideration of any acoustic dispersion, attenuation and reflection. The function of the pulse excitation added to the edges of the outer rectangle is $V(t)=100\,\mathrm{e}^{-(t-b)^2/2c^2}$, with $b=5\times10^{-7}$ and $c=1\times10^{-7}$.

3.1. Fluid model

When all of the targets are fluids, a fluid simulation model can be built. While the actual organism contains solid structures such as fluid and bone, all of the objects are considered to be equivalent to a fluid to simplify the modeling, create a geometric model of the tumor embedded in the normal tissue, and treat the bone as a fluid. The physical and acoustic properties were then set.

The fluid model shown in Fig. 3 should be analyzed based on the corresponding theoretical analysis described above, including electromagnetic field model and acoustic field model of fluid model. The rectangle on the right-hand side, which is used to simulate the cartilage, is regarded as a fluid. As for the physical and acoustic properties of the targets, the density of tissue is set to be 1 g/cm^3, the density of simulated cartilage is set to be 1.668 g/cm^3, the conductivity of simulated cartilage is set to be 0.15 S/m, and the speed of sound in simulated tissue is set to be 1481 m/s, and the speed of sound in simulated cartilage is set to be 1540 m/s.

Figure 4 shows the normalization results of our simulation. Figure 4(a) shows the thermo–acoustic source when $t=0.46$ μs. Figure 4(b) shows the current density modulus distribution when $t=0.46$ μs, and figure 4(c) shows the acoustic pressure distribution of the model when $t=10$ μs, with the acoustic pressure distributed throughout the fluid area. The normalized curves of the conductivity, thermo–acoustic source, current density modulus, and the y component of the electric field intensity along the central white straight line in Fig. 4(a) are shown in Fig. 4(d).The result shows that the heat absorption distribution and the thermo–acoustic source are related to the conductivity distribution. The thermo–acoustic source due to the Joule heating is distributed in the whole fluid area.

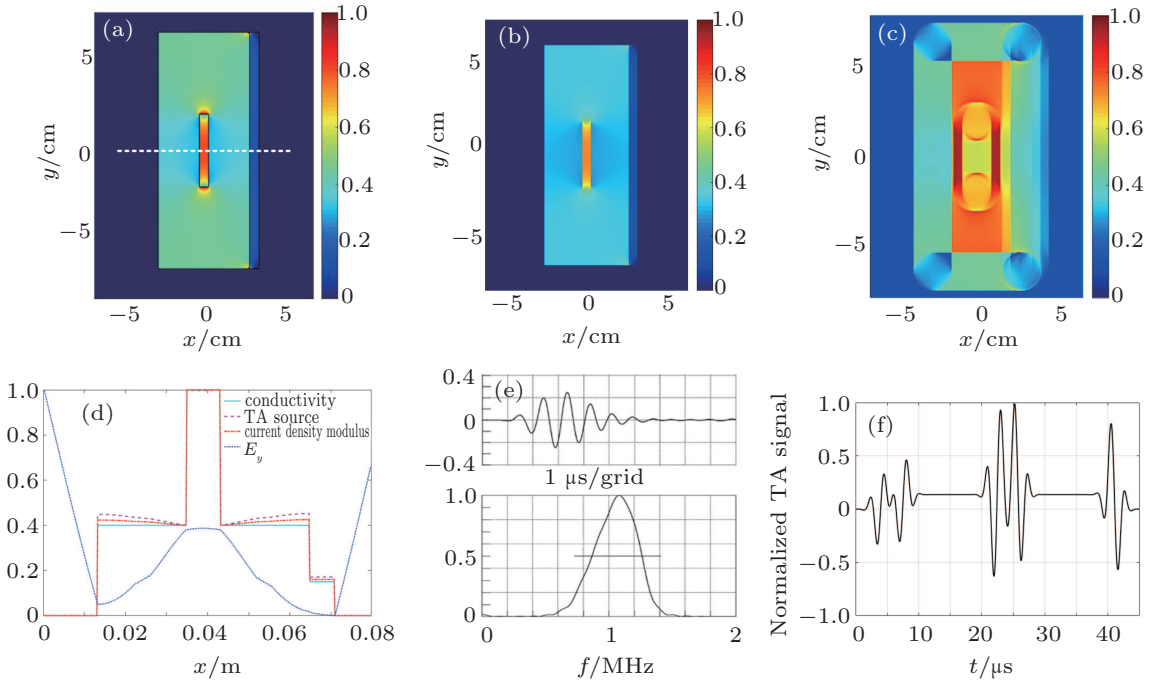


Fig. 4. The simulation results of the fluid model. (a) Thermo–acoustic source. (b) Current density modulus distribution. (c) Acoustic pressure distribution. (d) Conductivity, thermo–acoustic source, current density modulus, and the y component of the electric field intensity for the white straight line. (e) The impulse response and amplitude–frequency characteristic of the ultrasonic transducers. (f) Simulation convolved acoustic pressure waveform.

An acoustic signal is then excited due to thermal expansion. The distance between the data acquisition site and the center of the model is 0.035 m, which means that the position of the simulative transducer is at the point (0.035 m, 0 m). In practical experiments, the signals obtained by the transducers are actually the convolution between the impulse response of the ultrasonic transducers and the acoustic pressure. Consequently, the simulation signals are processed by the convolution to compare with experiments. The impulse response and amplitude–frequency characteristic of the ultrasonic transducers are shown in Fig. 4(e), figure 4(f) shows the convolved acoustic pressure wave for the white straight line in Fig. 4(a). There are five clusters in Fig. 4(f), indicating signals from different edges, the positions of the clusters are corresponding to the position of the change of the conductivity. The wave clusters begin at 3.375 μs and end at 40.5 μs, the corresponding time of the second cluster is 6.75 μs, the corresponding time of the third cluster is 21.0375 μs, and the corresponding time of the fourth cluster is 25.2 μs. The time of the first cluster is consistent with the propagation time of the acoustic wave from the right edge of the right rectangle model to the transducer, the time of the second cluster is consistent with the propagation time of the acoustic wave from the left edge of the right rectangle model to the transducer, the time of the third cluster is consistent with the propagation time of the acoustic wave from the right edge of the inner rectangle model to the transducer, the time of the fourth cluster is consistent with the propagation time of the acoustic wave from the left edge of the inner rectangle model to the transducer, and the time of the fifth cluster is consistent with the propagation time of the acoustic wave from the left edge of the outer rectangle model to the transducer. These results prove that the acoustic signals are caused by the different structures in the model and they reveal the conductivity variation of the model.

There is a cluster at the right-hand edge of the right-hand rectangle model in the acoustic pressure waveform. Based on the distances from edges to the transducer and speed of sound, we analyzed the acoustic propagation time from edge of model to the transducer and then compared the theoretical and simulation value. According to the theoretical calculation, the corresponding time of each cluster is 3.376 μs, 6.623 μs, 21.815 μs, 25.191 μs, 40.384 μs, and the results show that the simulation results are in good agreement with the theoretical value. Compared with the theoretical value the errors of the simulation results are 0.03%, 1.92%, 3.56%, 0.04%, and 0.29%, respectively, which proves the feasibility of our method.

The error is related to the calculation error and the result of acoustic pressure convolving with probe characteristic response. Even so, the numerical analysis result shows that the changes of the acoustic signal and the thermo–acoustic source reflect the conductivity changes of the object, the acoustic signal can reflect the anterior and posterior interface of simulative cartilage, and the positions of the clusters in the numerical results are basically consistent with the positions of electrical conductivity change.

3.2. Fluid–solid coupling model

The fluid–solid coupling model should be analyzed according to the corresponding theoretical analysis above, including the electromagnetic field model and the acoustic field model for fluid–solid coupling. The model is shown in Fig. 3, the outer rectangle is used to simulate normal tissue and the inner rectangle is used to simulate tumor tissue, which are considered to be fluids, and the rectangle on the right-hand side that is used to simulate the bone is regarded as solid. Since each part of the target has different physical and acoustic properties, the density of the fluid is set to be 1 g/cm^3, the speed of sound in fluid is set to be 1481 m/s, the conductivity of bone is set to be 0.02 S/m, the density of simulated bone is set to be 1.668 g/cm^3, and the speed of sound in simulated bone is set to be 1728 m/s.

Figure 5 shows the normalized simulation results of the fluid–solid coupling model. The instantaneous short pulse current excited Joule heating as thermo–acoustic source at 0.46 μs is shown in Fig. 5(a). Figure 5(b) shows the modular of current density distribution when $t = 0.46$ μs, figure 5(c) shows the acoustic pressure distribution of the model when $t = 10$ μs. The figure shows the acoustic pressure exists only in the fluid area. The normalized distributions of conductivity, the thermo–acoustic source, current density modulus, and the y component of the electric field intensity along the central white straight line in Fig. 5(a) are shown in Fig. 5(d). The results show that the thermo–acoustic source is closely related to the conductivity distribution.

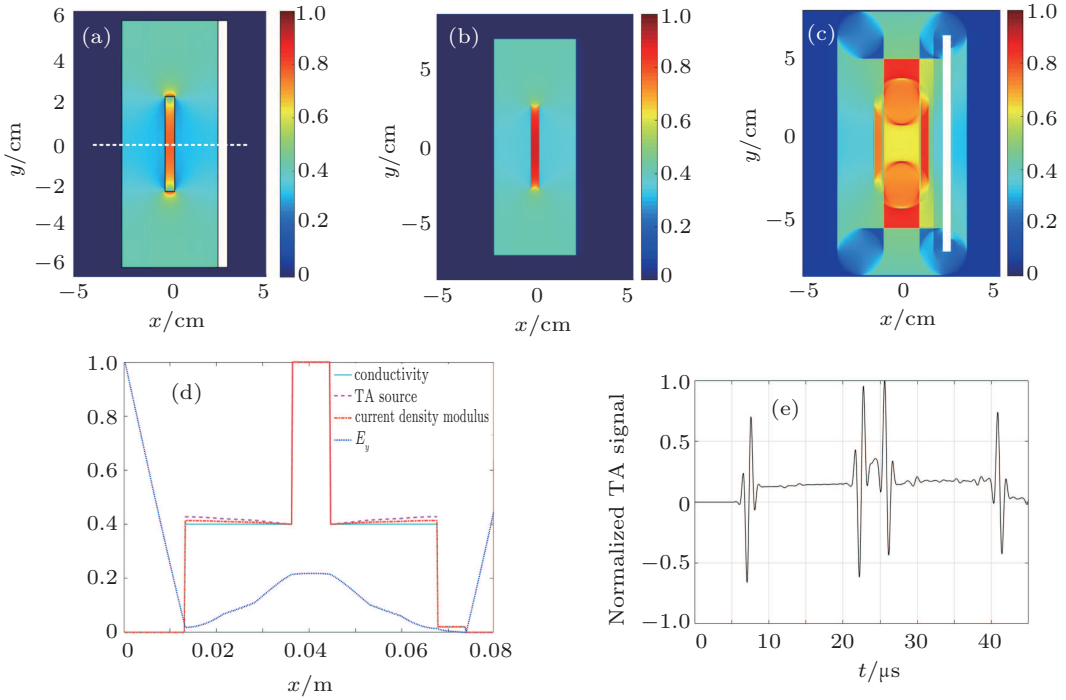


Fig. 5. The simulation results of the fluid–solid coupling model. (a) Thermo–acoustic source distribution. (b) Current density modulus distribution. (c) Acoustic pressure distribution. (d) Conductivity, thermo–acoustic source distribution, current density modulus, and the y component of the electric field intensity for the white straight line. (e) Simulation convolved acoustic pressure waveform.

The acoustic signal is then excited due to thermal expansion. The distance between the data acquisition site and the center of the model was 0.035 m. The signals obtained by the transducers are actually the convolution between the impulse response of the ultrasonic transducers and the acoustic pressure. The simulation signals were then processed with the convolution. Figure 5(e) shows the convolved acoustic pressure wave at the white straight line in Fig. 5(a). There exist four clusters, as shown in Fig. 5(e), which represent the signals from different edges of fluid targets. The position of every cluster corresponds to the site of conductivity change. The wave clusters begin at 6.1 μs and end at 40 μs, the corresponding time of the second cluster is 21.2 μs and the corresponding time of the third cluster is 25 μs. The time of the first cluster is consistent with the propagation time of the acoustic wave from the right edge of the outer rectangle model to the transducer, the time of the second cluster is consistent with the propagation time of the acoustic wave from the right edge of the inner rectangle model to the transducer, the time of the third cluster is consistent with the propagation time of the acoustic wave from the left edge of the inner rectangle model to the transducer, and the time of the fourth cluster is consistent with the propagation time of the acoustic wave from the left edge of the outer rectangle model to the transducer. These results demonstrate that the acoustic signals are caused by the different geometric model. They also reveal the conductivity changes of the model. There is no acoustic pressure occurrence in the hard bone area.

There is no cluster on the right-hand edge of the right-hand rectangle model in the acoustic pressure waveform. The acoustic propagation time from edge of object to the transducer can be analyzed according to the distances from edges to the transducer and speed of sound. By comparing theoretical analysis, simulated values and theoretical calculations, the corresponding times of each cluster are 6.27 μs, 21.462 μs, 24.838 μs, and 40.031 μs according to theoretical calculation. The results show that the simulation results are in good agreement with the theoretical value. Compared with the theoretical value, the errors of the simulation results are 2.71%, 1.22%, 0.65%, and 0.08% respectively, which confirm the feasibility of our method.

4. Experimental method

To verify the results of theoretical and simulation analysis, the TAI-CI experimental system as shown in Fig. 6 was established for experimental research.

The experimental system mainly includes four parts: excitation source system, ultrasonic detection system, scanning system, acquisition, and imaging system.

Excitation source system: The pulse excitation source system consists of the signal generation system, pulse source, and a pair of excitation sheet copper electrode. The signal generation system controls the working state of the pulse source by controlling the input square wave pulse signal of the pulse source. The power switching tube is used to realize the quick charge and discharge of energy storage capacitors. The pulse current is then generated and injected into the target body through the copper electrodes. The pulse width of the current is 0.5 μs ∼ 1 μs with the change of the load, and the voltage of the storage capacitor is 0 V ∼ 800 V, the discharge peak current can be continuously adjusted.

Acoustic signal detection system: The acoustic signal detection system mainly includes ultrasonic transducer, low noise preamplifier, filter and data acquisition system. The ultrasonic transducer is placed in a glass tank filled with insulating oil, and the transducer and the targets are at the same height. The acoustic signal is detected by the ultrasonic transducer with a center frequency of 1 MHz and the bandwidth of 0.87 MHz to 1.27 MHz. The signal was then amplified by 60-dB low noise preamplifier and filtered by 0.1 MHz∼3 MHz band pass filter. The acoustic pressure signals were then collected and stored. The pressure data will then be used to reconstruct the images.

Scanning system: The acoustic pressure signals were collected by B-scan. The scanning system is shown in Fig. 6, ultrasonic transducer can be controlled to move in the x, y, and z directions by rotating B, A, and C, respectively. The data acquisition in the three directions with stepping-mode can then be realized. In this paper, the transducer was moved in the step of 1 mm.

Imaging system: Imaging of the acoustic pressure and the thermo–acoustic source distribution is carried out by using the processed acoustic pressure signal.

Submerged inside insulating oil for acoustic coupling, the sample and the ultrasonic transducer are placed in a glass tank that is filled with insulating oil. The position of the target imaging is at the same level as the ultrasonic transducer.

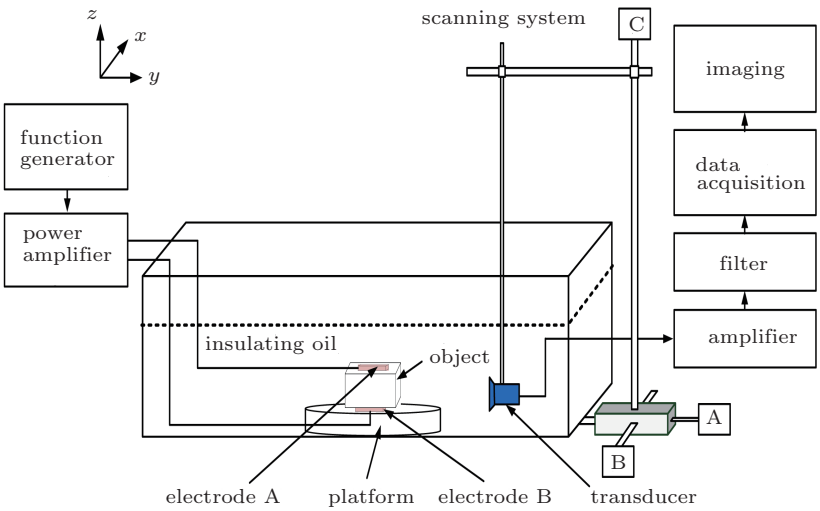


Fig. 6. Schematic diagram of the TAI-CI experimental system.

The instantaneous energy density and repetition frequency ensure tat there is enough energy density to produce sound. The matching between the dominant frequency of excitation source and that of the ultrasonic transducer is another important factor to detect the acoustic signals effectively.

A safety assessment was carried out. A phantom with a conductivity of 0.2 S/m was used for the experiment. The width of the pulse current was less than 1 μs, and the amplitude was adjusted from zero until the acoustic pressure signal can be detected by ultrasonic probe. The experiment shows

that the acoustic pressure signal can be detected when root-mean-square value of current is 6.708 mA, and this level of instantaneous short pulse excitation current used in the experiment is far less than the standard of human ventricular fibrillation or for damage to human organs. Finally, no harmful physiological effects occurred.

In the experiments, the 0.27% sodium chloride solution was mixed with agar powder and was then heated. The gel was then formed by cooling — the conductivity of this gel is 0.5 S/m. The gel was used to simulate biological tissue, the crescent cartilage and hard bone of pig were tightly attached on one side of the gel. The experimental research was then carried out to verify the effect of bone on acoustic signal detection and imaging.

As shown in Fig. 7(a), the crescent cartilage attached to the side of the gel phantom is shown in Fig. 7(b). The thickest portion of the crescent bone has a thickness of 5 mm. The length and width of the phantom are 12 cm and 5 cm, respectively. In the center location of the model a small rectangle phantom was cut away, the length and width of the rectangular hollow are 2 cm and 5 mm. This hollow is full of insulating oil.

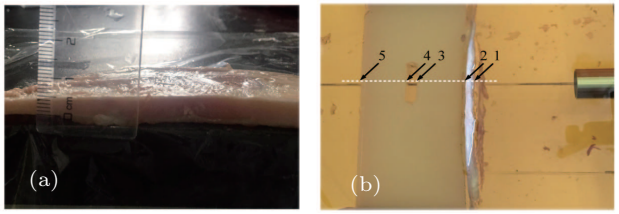


Fig. 7. Photographs of cartilage and phantom. (a) Crescent bone of the pig and (b) experimental photographs.

The hard bone used in the experiment is shown in Fig. 8(a). The hard bone attached on one side of the gel phantom is shown in Fig. 8(b). The thickness of the thinnest part of the hard bone is 5 mm, the thickness of the thickest part of the hard bone is 10 mm. The length and width of the phantom are 12 cm and 5 cm, respectively. In the center location of the model a small rectangle phantom was cut away. The length and width of the rectangular hollow are 2 cm and 5 mm. This hollow was full of insulating oil.

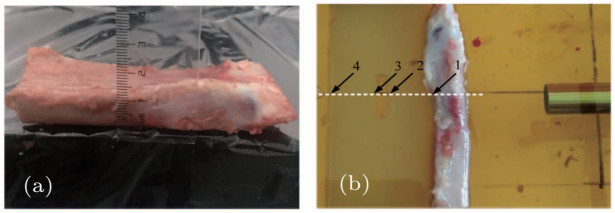


Fig. 8. Photographs of hard bone and phantom. (a) Hard bone of the pig and (b) experimental photographs.

A high voltage narrow pulse excitation source is used to inject pulse current into the target body through a pair of copper electrodes, the pulse width of pulse current is 0.8 μs and the repetition frequency is 80 Hz. Immediately after injecting current into the gel, joule heating is produced inside the gel which contains a certain concentration of sodium chloride. Due to the application of a transient short pulse, the heat conduction can be ignored. The Joule heat then excites the thermal expansion to generate ultrasonic signals, and the acoustic signals are received by the ultrasonic transducer.

Both experiments using the pure gel without bone shielding and the coupled bone shielding are carried out. The bone is located between the gel and the transducer, and it is tightly attached on the surface of the gel. The distance between this surface of the gel and the ultrasonic transducer is 5.5 cm.

5. Experimental results

5.1. Experimental results of the gel

The position of the ultrasonic transducer is shown in Fig. 7(b), and the ultrasonic transducer is perpendicular to the length direction of the gel. When the gel is not covered by bone, the acoustic signals are received by ultrasonic transducer and then are processed through preamplifier and filters. The waveform diagram of ultrasonic signal without bone is shown in Fig. 9, the first wave cluster appeared at 39 μs, because the ultrasonic transducer is 5.5 cm away from the boundary of the gel. The time of the first cluster is consistent with the propagation time of the acoustic wave from the right edge of the outer rectangle model to the transducer, subsequently, there are three more wave clusters in the process of sound signal propagation, the corresponding times of the three wave clusters were 54 μs, 57.5 μs, and 73 μs, respectively. The time of the second cluster is consistent with the propagation time of the acoustic wave from the right-hand edge of the inner rectangular hollow model to the transducer, the time of the third cluster is consistent with the propagation time of the acoustic wave from the left-hand edge of the inner rectangular hollow model to the transducer, and the time of the fourth cluster is consistent with the propagation time of the acoustic wave from the left-hand edge of the outer rectangular model to the transducer.

In Fig. 9, the first cluster and the fourth cluster correspond to the two boundaries of outer gel, whose width was 5 cm. The time difference between the ultrasonic signal propagating from these two boundaries to the ultrasonic transducer is 34 μs, and the speed of sound for insulating oil is 1425 m/s. In theory, the time difference between the ultrasonic signal propagating from these two boundaries to the ultrasonic transducer and the time of ultrasonic propagation from the outer boundary of the gel to the ultrasonic transducer should be

$$\Delta t_1 = \frac{d}{v} = \frac{0.05\ \text{m}}{1425\ \text{m/s}} = 35.09\ \mu\text{s}, \tag{23}$$

$$\Delta t_2 = \frac{d}{v} = \frac{0.055\ \text{m}}{1425\ \text{m/s}} = 38.6\ \mu\text{s}. \tag{24}$$

In comparison with the theoretical results, the experimental time difference between the ultrasonic signal propagating from these two boundaries to the ultrasonic transducer is 34 μs and the propagation time of the acoustic wave from the right outer boundary of the gel model to the transducer is 39 μs. There is a certain error due to the measurement errors including the size of gel and the position of the ultrasonic transducer. However, it can be considered that the experimental value is basically consistent with the theoretical value.

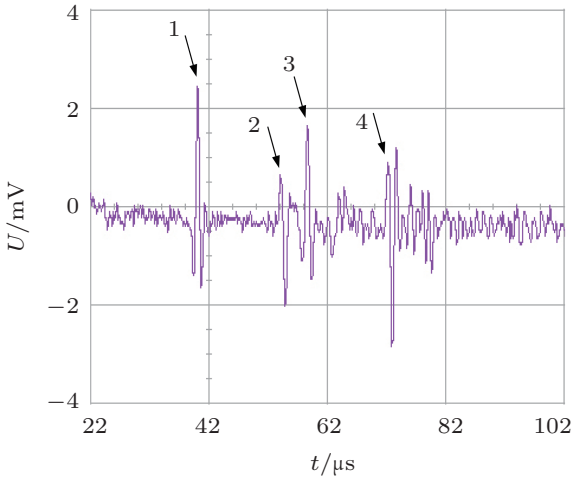


Fig. 9. Waveform diagram of ultrasonic signal without bone.

5.2. Experimental results of gel and cartilage

An experiment was performed to verify the effect of cartilage on the TAI-CI ultrasonic signal, as shown in Fig. 7(b). The applied pulse excitation parameters remain the same, and the ultrasonic signal is collected and processed, as shown in Fig. 10.

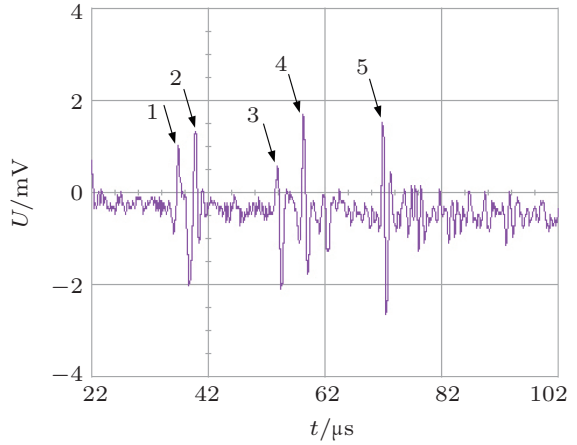


Fig. 10. Waveform diagram of ultrasonic signal with the cartilage.

It can be seen in Fig. 10 that there are five clusters in the waveform profile. The time of the first cluster is consistent with the propagation time of the acoustic wave from the outer boundary of the cartilage to the transducer. The position of the second cluster is basically the same as that of the first cluster in Fig. 9, which means the position of the second wave cluster in Fig. 10 is consistent with the boundary between cartilage and gel. The positions of the third and the fourth wave clusters in Fig. 10 are consistent with the propagation times that the acoustic wave propagates from the two boundaries of the inner rectangle hollow to the transducer. The position of the last cluster is consistent with the propagation time that the acoustic wave propagates from the last edge of the target to the transducer. The positions of the five clusters in the waveform are consistent with the theoretical calculation value of sound wave propagation. It can be seen from Fig. 10 that the amplitude of detected acoustic signal does not decrease significantly, which means that the presence of cartilage does not affect the signal detection.

The height of the ultrasonic transducer in the insulating oil is kept constant.The transducer is moved in the length direction of the gel in the step of 1 mm. The acoustic signals are then collected and processed. Finally, the normalized image is reconstructed using processed data, as shown in Fig. 11.

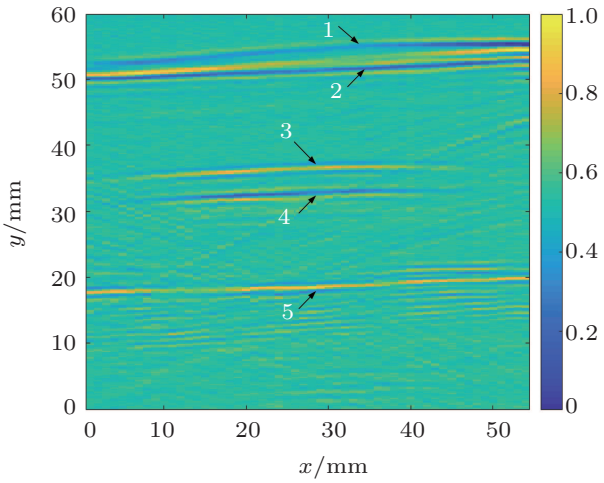


Fig. 11. The B-scan image of the cartilage and phantom.

The result shows that the image structure is in agreement with the original photograph of the phantom and cartilage structure in Fig. 7(b). The position of the inner rectangle hollow with different conductivity can be obtained. From the photograph shown in Fig. 7(b), it can be seen that the middle position of the cartilage is compacted with the gel phantom but the two ends of the cartilage are thin and slightly upturned. Then, there is insulating oil between the gel and the ends of the cartilage, which corresponds with Fig. 11. There are two boundaries in the position where the cartilage is attached to the gel more tightly, which means that the anterior and posterior interface of the cartilage itself can be identified. There are three boundaries at the ends of the cartilage. By comparing Fig. 11 with Fig. 7(b), the B-Scan images obtained can accurately reflect the distribution of cartilage and gel with different conductivity. The image results further illuminate that

the signals are generated by the abrupt pressure changes at conductivity boundaries.

5.3. Experimental results of gel and hard bone

For thicker hard bone and lower electrical conductivity, the experiment was carried out using gel phantom and hard bone. The applied pulse excitation parameters remained the same. The acoustic signal was obtained as a means of evaluating the impact of the hard bone. The waveform diagram of ultrasonic signal and the B-scan image are shown in Figs. 12 and 13. respectively.

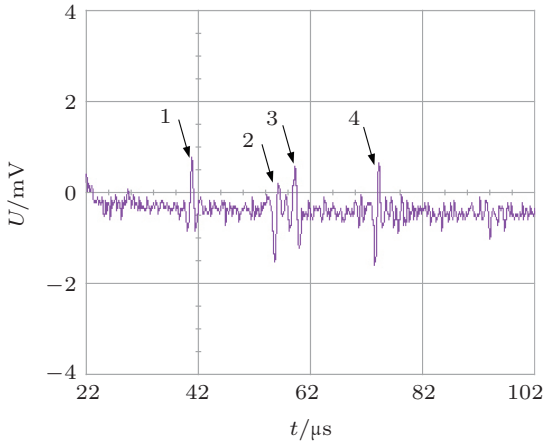


Fig. 12. Waveform diagram of ultrasonic signal with the hard bone.

There are four clusters. The position of each cluster corresponds to the boundaries of the outer and inner rectangle models. The amplitude of ultrasonic signal in Fig. 12 has a downward trend.

Images of samples were also obtained using the B-Scan approach, the transducer was moved in the length direction of the gel in the step of 1 mm, and the acoustic signals were collected and processed. The normalized image was then reconstructed using collected data, as shown in Fig. 13. Although the hard bone plays a certain role in attenuating the acoustic signal, a clear normalized image can still be obtained, and the image can reflect the position of the conductivity change of the sample.

In conclusion, By comparing Fig. 9 with Fig. 10, we can see that the results of cartilage test agree well with the simulation results of the pure fluid model, the acoustic signal can reflect the anterior and posterior interface of cartilage, and there is slight attenuation of the acoustic signal in the experiment including cartilage. The results of the hard bone experiment are consistent with the simulation results of the fluid-solid coupling model. The acoustic signal can only reflect the posterior interface of hard bone. By comparison with Fig. 9 and Fig. 10, the amplitude of ultrasonic signal in Fig. 12 has a downward trend, indicating that the harder and thicker bone weakens the acoustic signal. However, the acoustic signal wave clusters still clearly reflect the characteristics of ultrasonic signal propagation from different positions of the target to the ultrasonic transducer.

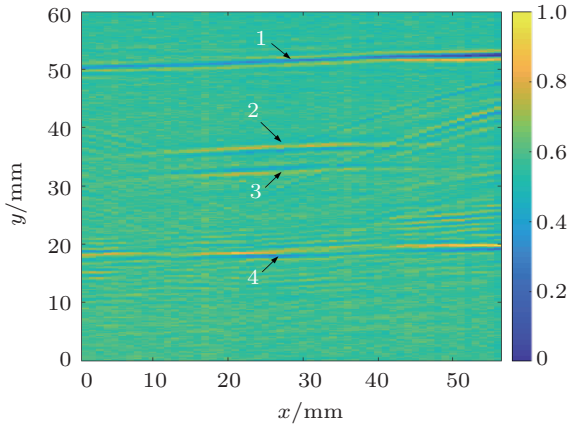


Fig. 13. The B-scan image of the hard bone and phantom.

6. Conclusion

In this paper, we highlighted the potential of the TAI-CI as a new method for cancer detection. The basic principle, simulation for both of pure fluid and fluid–solid coupling models, and experiment including cartilage and hard bone are reported in this paper. This research indicates that the results of cartilage test agree well with the simulation results of pure fluid model. The acoustic signal can reflect the anterior and posterior interface of cartilage, which illustrates the crescent cartilage selected in this paper can be equivalent to the fluid. The conductivity of cartilage has difference with outer rectangle gel and insulating oil. Meanwhile the results of the hard bone experiment are consistent with the simulation results of the fluid–solid coupling model, which means that the hard bone should be regarded as a solid in the simulation analysis. Consequently, our theoretical analysis, simulation results, and data from proof-of-concept experiments provide a more accurate interpretation of the difference in thermo–acoustic signals between the two targets. The structure distribution of gel with different conductivity shown by the B-scan can confirm that the imaging can reflect the variation of electrical parameters of target. The validity and reliability analytical methods for the pure fluid and the fluid–solid model have been verified. We will further study the reconstruction of conductivity based on this improved model.

The simulation and experiments on cartilage and hard bone combined with low electrical conductivity gel verify the feasibility of TAI-CI for low conductivity target and biological tissue target, even with bone shielding. This benefits from the thermo–acoustic signal, which is attenuated only during the outward propagation. This provides a basis for further study on the reconstruction of conductivity images of complex biological tissues. The imaging of brain tumors, liver cancers, and

breast cancer can be considered as further applications of this imaging system. This method and system will promote the application of multiple physical field coupled imaging technology in the early diagnosis of these diseases.

Acknowledgment

Li Yan-Hong would like to thank Mr. Tong J Z for useful discussions about the numerical simulation and experimental study.

References

[1] Fear E C, Meaney P M and Stuchly M A 2003 *IEEE Potentials* **22** 12
[2] Wang X, Bauer D R, Witte R and Xin H 2012 *IEEE Trans. Biomed. Eng.* **59** 2782
[3] Prakash S, Karnes M P, Sequin E K, West J D, Hitchcock C L, Nichols S D, Bloomston M, Abdel-Misih S R, Schmidt C R, Martin E W Jr, Povoski S P and Subramaniam V V 2015 *Physiol. Meas.* **36** 315
[4] Skourou C, Hoopes P J, Strawbridge R R and Paulsen K D 2004 *Physiol. Meas.* **25** 335
[5] Brindle K 2008 *Nat. Rev. Cancer* **8** 94
[6] Liu G D and Zhang Y R 2011 *Acta Phys. Sin.* **60** 074303 (in Chinese)
[7] Halter R J, Schned A, Heaney J, Hartov A, Schutz S and Paulsen K D 2008 *J. Urol.* **179** 1580
[8] Metherall P, Barber D C, Smallwood R H and Brown B H 1996 *Nature* **380** 509
[9] Halter R J, Hartov A and Paulsen K D 2008 *IEEE Trans. Biomed. Eng.* **55** 650
[10] Wang S H, Tao C and Liu X J 2013 *Chin. Phys. B* **22** 074303
[11] Cheng R X, Tao C and Liu X J 2015 *Chin. Phys. B* **24** 114301
[12] Murphy E K, Mahara A and Haler R J 2017 *IEEE Trans. Med. Imaging* **36** 892
[13] Wu D, Tao C, Liu X J and Wang X D 2012 *Chin. Phys. B* **21** 014301
[14] Jin X, Li C and Wang L V 2008 *Med. Phys.* **35** 3205
[15] Lou C, Yang S, Ji Z, Chen Q and Xing D 2012 *Phys. Rev. Lett.* **109** 218101
[16] Xu Y and He B 2005 *Phys. Med. Biol.* **50** 5175
[17] Guo G P, Ding H P, Dai S J and Ma Q Y 2017 *Chin. Phys. B* **26** 084301
[18] Guo L, Liu G Q and Xia H 2015 *IEEE Trans. Biomed. Eng.* **62** 2114
[19] Liu G Q, Huang X, Xia H and Wu S Z 2013 *Chin. Sci. Bull* **58** 3600
[20] Xu M and Wang L V 2002 *Med. Phys.* **29** 1661
[21] Liu L B, Tao C, Liu X J, Li X L and Zhang H T 2015 *Chin. Phys. B* **24** 024304
[22] Feng X, Gao F and Zheng Y 2013 *Appl. Phys. Lett.* **103** 083704
[23] Ji Z, Lou C, Yang S and Xing D 2012 *Med. Phys.* **39** 6738
[24] Li Y, Liu G, Xia H, Xia Z and Yang Y 2018 *IEEE Trans. Magn.* **54** 5100604
[25] Yang Y, Xia Z, Li Y, Xia H, Liu G and Yan X 2018 *Sci. Sin. Tech.* **48** 48
[26] Shi Y, Qin H, Yang S and Xing D 2016 *Nano Res.* **9** 3644
[27] Yan B, Qin H, Huang C, Li C, Chen Q and Xing D 2017 *Opt. Lett.* **42** 1253
[28] Zhou W, Chen Z, Yang S and Xing D 2017 *Opt. Lett.* **42** 2145
[29] Feng X, Gao F, Kishor R and Zheng Y 2015 *Sci. Res.* **5** 11489
[30] Chaudhary S S, Mishra R K, Swarup A and Thomas J M 1984 *Indian J. Biochem. Biophys.* **21** 76
[31] Ku G and Wang L V 2000 *Med. Phys.* **27** 1195
[32] Li Y, Liu G, Yang Y and Xia Z 2018 *J. Med. Imag. Health. In.* **8** 134
[33] Xu M, Xu Y and Wang L V 2003 *IEEE Trans. Biomed. Eng.* **50** 1086
[34] Zhigilei L V and Garrison B J 2000 *J. Appl. Phys.* **88** 1281
[35] Nan H and Arbabian A 2017 *IEEE Trans. Microw. Theory Techn.* **65** 2607
[36] Omar M, Kellnberger S, Sergiadis G, Razansky D and Ntziachristos V 2012 *Med. Phys.* **39** 4460
[37] Gabriel S, Lau R W and Gabriel C 1996 *Phys. Med. Biol.* **41** 2251
[38] Gabriel S, Lau R W and Gabriel C 1996 *Phys. Med. Biol.* **41** 2271
[39] Kellnberger S, Hajiaboli A, Razansky D and Ntziachristos V 2011 *Phys. Med. Biol.* **56** 3433
[40] Hu G, Li X and He B 2010 *Appl. Phys. Lett.* **97** 103705
[41] Joines W T, Zhang Y, Li C and Jirtle R L 1994 *Med. Phys.* **21** 547
[42] Cheng Y and Fu M 2018 *Med. Sci. Monit.* **24** 1276
[43] Wan Y, Borsic A, Heaney J, Seigne J, Schned A, Baker M, Wason S, Hartov A and Halter R 2013 *Med. Phys.* **40** 063102